CrossMark

Layered Bi_2MoO_6/LDH hetero-structured composites with enhanced visible light photocatalytic activity

Fengxian Hu[1,2] · Entian Cui[1] · Hongxia Liu[1] · Jing Wu[1] · Yong Dai[1] · Guiyun Yu[1]

Abstract

Series of Bi_2MoO_6/NiAl-LDH hetero-junction photocatalysts were synthesized by a two-step hydrothermal method with a self-assembled process. It indicated that the in-situ intercalated NiAl-LDH showed a tight contact with Bi_2MoO_6 layers and thus exhibited the rapid transfer of photogenerated electrons on the interface. The photocatalytic performance was evaluated by the degradation of rhodamine B (RhB) under visible light irradiation. The resulted Bi_2MoO_6/NiAl-LDH sample showed a higher visible-light photocatalytic activity for the degradation of RhB than any single component. The optimal LDH content in Bi_2MoO_6/NiAl-LDH is 15% with the degradation efficiency for more than 90% during 60 min. The excessive amount of NiAl-LDH in Bi_2MoO_6/NiAl-LDH could reduce the light absorption efficiency of Bi_2MoO_6 and thus affected the generation of photoinduced electron–hole pairs. The enhanced photocatalytic activity and stability of Bi_2MoO_6/NiAl-LDH was attributed to the synergistic effects of the introduction of narrow band-gap NiAl-LDH and the construction of layered hetero-junction. Our synthetic method of self-assembly sheets has certain guided significance for the synthesis and application of other photocatalysts.

1 Introduction

The ecological environment is closely related to people's lives. The leap-forward development of the economy had emitted a large number of toxic pollutants [1], which has a significant impact on the environment. Therefore, the problems of purifying and repairing environmental pollution needed to be solved [2–4].

Recently, the most studied bismuth-based photocatalysts include Bi_2O_3 [5], Bi_2S_3 [6, 7], $BiVO_4$ [8, 9], Bi_2WO_6 [10, 11], $Bi_4Ti_3O_{12}$ [12, 13] etc. Among those Bi-based photocatalysts, the bismuth molybdate mainly include α-$Bi_2Mo_3O_{12}$,

✉ Yong Dai
  123daiyong123@163.com

✉ Guiyun Yu
  yuguiyun1@163.com

1   School of Chemistry & Chemical Engineering, Yancheng Institute of Technology, Yancheng 224051, People's Republic of China

2   School of Chemistry & Chemical Engineering, Jiangsu University, Zhenjiang 212013, People's Republic of China

β-$Bi_2Mo_2O_9$ and γ-Bi_2MoO_6 [14], in which only γ-Bi_2MoO_6 shows a layered Aurivillius structure with a similar sandwiched structure in the $Bi_2O_2^{2+}$ unit and a point-adjacent MoO_6 octahedral sandwich [15, 16]. The strong interaction between Bi 6s and O 2p orbitals reduces the symmetry of the structure and thus makes it have a higher oxidation activity and photocatalytic activity [17]. Recent results revealed that Bi_2MoO_6 has a narrow band gap, which has the potential for visible light absorption. However, the low absorption efficiency and a high recombination rate of charge carriers at the interface limited the application of Bi_2MoO_6. Thus, many efforts have been paid to improve the photocatalytic activity of Bi_2MoO_6 by controlling morphological structures, elemental doping and constructing hetero-junctions. Because the photocatalytic performance is closely related to the structure of photocatalyst, a series of Bi_2MoO_6 with various structural features have been prepared to achieve the high photocatalytic efficiency [18–21]. The doping of rare earth elements in Bi_2MoO_6 [22–25] is also a method for enhancing the photocatalytic activity of Bi_2MoO_6. Furthermore, combining Bi_2MoO_6 with other semiconductor materials to construct hetero-junctions has been regarded as the most effective way to improve photocatalytic activity, such as: $BiOI$/Bi_2MoO_6 [26], Bi_2O_3/Bi_2MoO_6 [27], $Bi_2O_2CO_3$/Bi_2MoO_6 [28], g-C_3N_4/Bi_2MoO_6 [29] etc.

Layered double hydroxide (LDH) is the typical layered anionic clay with a regular octahedral structure similar to brucite, which has been regarded as the efficient photocatalyst due to the low cost, simple preparation and highly photocatalytic efficiently [30, 31]. Its general formula is $[M_{1-x}^2 + M_x^3(OH)_2]^{x+} (A^{n-})_{x/n} \cdot yH_2O$, where M^{3+} represents a divalent cation, M^{2+} represents a trivalent cation, and A^{n-} represents an interlayer anion, $x = M^{2+}/(M^{2+} + M^{3+})$. LDH is a semiconductor photocatalyst material for photocatalytic water decomposition and environmental pollutant degradation due to its large surface area, interlayer anion exchangeability and a large amount of hydroxyl groups [32–35].

The layered structure semiconductor material has a high layer charge density, a parallel two-dimensional interlayer space and effective contact between the layers by means of interlayer electrostatic interaction, which is favorable for electron transport. Therefore, the photocatalytic activity can be effectively improved. In recent years, some researchers have attempted to enhance photocatalytic activity of bismuth molybdate by combining with hydrotalcite to construct hetero-junctions, such as: BiOCl/NiFe-LDH [36], g-C$_3$N$_4$/NiFe-LDH [37], g-C$_3$N$_4$/CuONP/LDH [38] and so on. However, there are few reports about the hetero-junction of hydrotalcite and bismuth molybdate.

Therefore, we attempt to synthesize layered Bi$_2$MoO$_6$/NiAl-LDH semiconductor composites by a two-step hydrothermal method with the self-assembly of nickel-aluminum hydrotalcite and bismuth molybdate nano-layer. NiAl-LDH not only tunes the band structure of Bi$_2$MoO$_6$ to widen the absorption into visible light region, but also reduces the recombination rate of photogenerated electron–hole pairs and accelerates the charge transfer rate. The Bi$_2$MoO$_6$/NiAl-LDH composite shows a high efficiently for degrading RhB under visible light irradiation.

2 Experimental section

2.1 Materials

Aluminum nitrate nonahydrate (Al(NO$_3$)$_3$·9H$_2$O, AR, 99.0%), nickel nitrate hexahydrate (Ni(NO$_3$)$_2$·6H$_2$O, AR, 98%), carbamide (CH$_4$N$_2$O, AR, 99%)and ammonium fluoride (NH$_4$F, AR, 98%) were purchased from Shanghai Aladdin Biochemical Technology Co., Ltd. Bismuth nitrate pentahydrate (Bi(NO$_3$)$_3$·5H$_2$O, AR, 99.0%), sodium molybdate dehydrate (Na$_2$MoO$_4$·2H$_2$O, AR, 99.0%), sodium hydroxide (NaOH, AR, 96.0%), ethanol absolute (CH$_3$CH$_2$OH, AR, 99.7%) and nitric acid (HNO$_3$, AR, 65–68%) were purchased from Shanghai Sinopharm Chemical Reagent Co., Ltd. Double distilled water was used throughout this study. All the chemicals were used without further purification.

2.2 Preparation of photocatalysts

Pure Bi$_2$MoO$_6$ was synthesized by a hydrothermal method according to the previous literature [39]. In a typical synthetic process, 6 mmol of Bi(NO$_3$)$_3$·5H$_2$O and 3 mmol of Na$_2$MoO$_4$·2H$_2$O were added into the mixed solution of distilled water (50 mL) and dilute HNO$_3$ (1 M, 2 mL) under the magnetic stirring to form a clear solution. The pH value of the precursor solution was adjusted to pH 5 by dropwise adding NaOH (2 M) solution. The whole mixture was transferred into an 80 mL capacity stainless steel Teflon-lined autoclave, and then heated at 180 °C for 24 h. After the reaction, it was naturally cooled to room temperature. The resulted precipitate was washed with distilled water and absolute ethanol for several times, and then dried at 80 °C for 12 h.

To synthesize Bi$_2$MoO$_6$/LDH composite, 0.5 g of Bi$_2$MoO$_6$ was dispersed into 60 mL of distilled water with a ultrasonic treatment for 1 h, and then 6 mmol of Ni(NO$_3$)$_2$·6H$_2$O, 2 mmol of Al(NO$_3$)$_3$·9H$_2$O, 8 mmol of NH$_4$F and 15 mmol of CH$_4$N$_2$O was respectively added into the above suspension under continuous stirring for 1 h. The resulted mixed suspension was transferred into a sealed Teflon-lined autoclave (80 mL), and then heated at 120 °C for 48 h. The resultant product was washed with distilled water and absolute ethanol for several times and dried in an oven at 80 °C for 12 h. A series of Bi$_2$MoO$_6$/LDH-x were prepared by a similar procedure, and labeled as Bi$_2$MoO$_6$/LDH-5, Bi$_2$MoO$_6$/LDH-10, Bi$_2$MoO$_6$/LDH-15, Bi$_2$MoO$_6$/LDH-20, Bi$_2$MoO$_6$/LDH-25, respectively, where x represent the NiAl-LDH content in Bi$_2$MoO$_6$/LDH composite of 5, 10, 15, 20 and 25 wt%.

2.3 Materials characterization

The crystalline phase and composition of the synthetic material were identified by X-ray powder diffractometer (XRD) on the Shimadzu XRD-6000 with Cu Kα radiation ($\lambda = 1.5406$ Å) at a scanning rate of 8°·min^{-1} in the 2θ range of 5–80° at 40 KV and 40 mA. The Fourier transform infrared spectra (FT-IR) were recorded with a NICOLET IS-10 using KBr disk method in the frequency range of 400–4000 cm^{-1} at room temperature. The morphology was measured by a FEI QUANTA 200 Scanning electron microscopy (SEM) attached with an energy dispersive X-ray spectrometer (EDS) operated at 5.0 KV. Transmission electron microscopic (TEM) and high resolution transmission electron microscopic (HR-TEM) images were carried out on JEM-2100 at an acceleration voltage of 200 kV. The specific surface areas of the samples were analyzed by Beckman Coulter SA 3100

at 77 K according to N_2 adsorption–desorption isotherms by means of the Brunauer–Emmett–Teller (BET) method. The binding energies of Bi, Mo, O, C, Al and Ni of the synthetic material were measured by X-ray photoelectron spectra (XPS), which was carried out by a Thermoelectric Inc., ESCALAB 250Xi photoelectron spectrometer using Al Kα radiation as the source and 284.6 eV as the adventitious C1s peak. The optical properties of samples were measured by a Shimadzu UV-3600 UV–Vis spectrophotometer (UV–Vis) using $BaSO_4$ as a reference in the region of 200–800 nm. The photoluminescence (PL) spectra were detected by a JASCO FP 6500 fluorescence spectrometer using a He-Cd laser source in the excitation wavelength of 325 nm.

The electrochemical measurements were conducted on an electrochemical station (Shanghai Chenhua CHI-660D) using a standard three electrode cell of a Pt counter electrode, an Ag/AgCl as reference electrode, and a conductive glass as working electrode. The conductive glass was respectively ultrasonically cleaned in distilled water, absolute ethanol and acetone for 30 min and dried at 60 °C for 12 h. A 40 mg sample was firstly added into 50 mL of acetone solution, and then sealed and ultrasonically dispersed for 1 h. The homogeneous suspension was spin-coated on the FTO glass electrode and dried at 60 °C for 12 h. The photocurrent was measured under a visible light irradiation of a 125 W xenon lamp equipped with a 420 nm cutoff filter at a bias voltage of 0.5 V, and immerged into 0.5 M Na_2SO_4 electrolyte solution. The electrochemical impedance spectroscopy (EIS) was measured using a mixed solution of 0.1 M KCl, 5 mM $K_3[Fe(CN)_6]$, and 5 mM $K_4[Fe(CN)_6]$ as an electrolyte solution.

2.4 Evaluation of photocatalytic activity

The photocatalytic activity of the obtained samples was evaluated by the degradation of RhB solution under visible light irradiation using a 300 W Xenon lamp ($\lambda \geq 420$ nm by a UV light filter). The specific process of the experiment was as follows: 0.1 g of the sample was dispersed into 200 mL of RhB solution with a concentration of 5 mg L^{-1} under continuous magnetic agitation for 30 min in the dark in order to ensure the adsorption–desorption equilibrium. During the visible-light illumination, approximately 5 mL of solution was taken out from the reaction suspension at 15 min intervals. The solution was centrifuged to remove the precipitate after the reaction. The RhB concentration of supernatant liquor was analyzed by a UV–Vis spectrophotometer (Shimadzu UV-3600) under the maximum absorbance wavelength at 554 nm. The degradation efficiency (η) of RhB was calculated by formula: $\eta = (C_0 - C_t)/C_0 \times 100\%$ where C_0 was the initial concentration of RhB and C_t was the concentration of RhB solution at time t.

With regard to the photocatalytic stability experiments, the catalyst was recollected by centrifugation, abstersion, and desiccation. Then, the sample was re-dispersed in the same concentration and volume of RhB aqueous solution. Other experimental process was repeated for four times, which was similar to the above photocatalytic test.

2.5 Active species trapping

Different active scavengers of 10 mM isopropanol, 10 mM benzoquinone, 10 mM sodium oxalate and 10 mM potassium dichromate were related to $\cdot OH$, $\cdot O_2^-$, h^+ and e^-, respectively [29, 40]. In order to understand the main roles of the active species in the photocatalytic experiment, those of four scavengers were added into the RhB aqueous solution, respectively. Then, the next experimental processes were similar to the above photocatalytic test.

3 Results and discussion

3.1 XRD analysis

The crystal phase and crystallinity of the prepared samples were measured by means of XRD patterns as shown in Fig. 1. Figure 1a shows the XRD pattern of NiAl-LDH, which is agreed with the octahedron phase of NiAl-LDH (JCPDS: 15-0087). Some characteristic diffraction peaks at 2θ values of 11.42°, 23.02°, 34.66°, 39.20° and 46.47° can be clearly observed, which are indexed to (003), (006), (012), (015) and (018) planes, respectively. Figure 1c shows the characteristic orthorhombic structure of Bi_2MoO_6
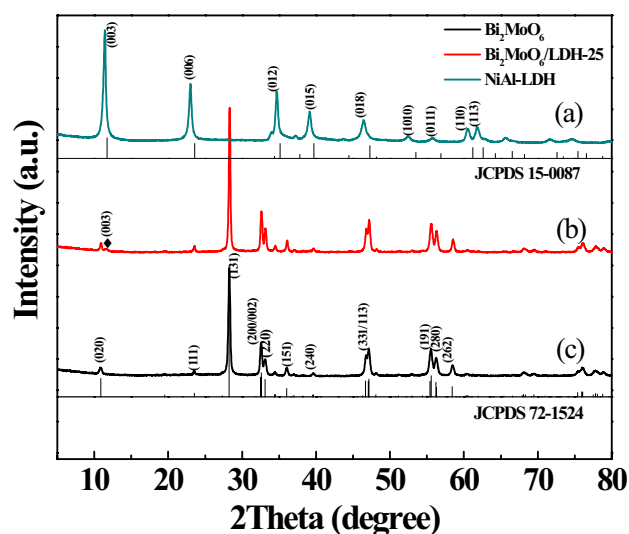

Fig. 1 XRD patterns of the composite (a) NiAl-LDH, (b) Bi_2MoO_6/LDH-25, (c) Bi_2MoO_6

(JCPDS: 72-1524), in which some diffraction peaks at 2θ values of 28.25°, 32.56°, 47.16° and 55.53° are related to the (131), (200), (113) and (191) planes, respectively. The diffraction peak intensity of Bi_2MoO_6 in Fig. 1b is higher than that of pure Bi_2MoO_6 due to the addition of NiAl-LDH. Only the diffraction peak of the (003) crystal plane can be seen in Fig. 1b, because the Bi_2MoO_6 nanosheets are pre-existing in the reaction solution, the LDH does not have enough time to form regular nanosheets, but directly forms the Bi_2MoO_6/LDH heterojunction. This is the main reason for the decrease in LDH crystallinity, and the results of the FE-SEM further verify this point. And when the compounding amount of LDH is less than 25 wt%, the characteristic diffraction peak of LDH was not observed in the XRD spectrum. Therefore, the content of NiAl-LDH in Bi_2MoO_6/LDH is also closely related to the characteristic peaks [41, 42]. The diffraction patterns of Bi_2MoO_6/LDH-25 composites have not unmatched diffraction peaks, indicating that no other impurities are formed.

3.2 FT-IR analysis

Figure 2 shows Fourier transform infrared spectra of Bi_2MoO_6, NiAl-LDH and Bi_2MoO_6/LDH-15. As shown in Fig. 2a, the absorption peaks at 3451, 1636 and 1380 cm^{-1} are assigned to the tensile vibration of –OH, the deformation vibration of H–O–H and NO_3^- stretching vibration [43], respectively. The absorption peak at 1050 cm^{-1} (Fig. 2b) is attributed to the adsorbed CO_2 by Bi_2MoO_6 [44]. The absorption peaks at 741 cm^{-1} and 591 cm^{-1} in Fig. 2a are lattice vibrations of Ni(Al)–O and O–Ni(Al)–O, respectively [45]. The absorption peaks at 842, 797 and 738 cm^{-1} (Fig. 2b) are attributed to the stretching vibration of Mo–O bond in MoO_6^{6-}, and 572 as well as 448 cm^{-1} (Fig. 2c) are attributed to telescopic vibration of the Bi–O
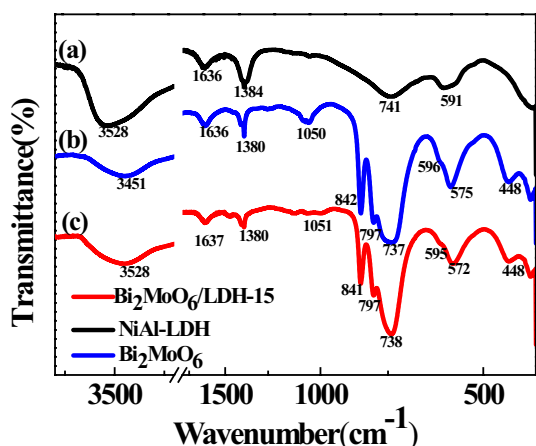
bond, respectively [29]. The corresponding absorption peak intensities of NiAl-LDH and Bi_2MoO_6 in Fig. 2c are weaker than those of in Fig. 2a, b due to the presence of the interaction between Bi_2MoO_6 and NiAl-LDH. Fig. S1 shows the Fourier transform infrared spectra of Bi_2MoO_6/LDH with different LDH contents, indicating that its structure has not been damaged.

3.3 Morphology

The morphology of NiAl-LDH, Bi_2MoO_6 and Bi_2MoO_6/LDH-15 composite were characterized using SEM and TEM. As shown in Fig. 3a, b, the SEM images of Bi_2MoO_6 consist of many irregular stacked nanosheets with the thickness of 30–35 nm. Figure 3c, d show flower-like structure of NiAl-LDH, which are composed of the cross-linking of the nanosheets with thickness of 35–50 nm. It indicates that such as flower-like structure increases the separation of the photonic electron pairs for the nanosheets. As shown in Fig. 3e, f, the Bi_2MoO_6/LDH is assembled by using in-situ growth of NiAl-LDH nanosheets on deposited on the surface of Bi_2MoO_6. The close contact between NiAl-LDH and Bi_2MoO_6 is favorable for the efficient transport of photoexcited electrons and holes between two components.

According to the HRTEM image of Bi_2MoO_6/LDH-15 in Fig. 4a, b, it can be obviously observed that two components are superimposed and intimately contacted. Moreover, the Bi_2MoO_6/LDH-15 composite shows the similar morphology and superstructure with the pure Bi_2MoO_6. Figure 4c shows an enlarged electron microscope in view of bismuth molybdate of the red frame in Fig. 4b. As shown in Fig. 4c, there are two sets of interplanar spacing of lattice fringes of 0.257 and 0.238 nm, corresponding to the (022) and (221) planes of Bi_2MoO_6, respectively. The selected black frame in Fig. 4b belongs to the NiAl-LDH, and the interplanar spacing of lattice fringes at 0.257 and 0.226 nm (Fig. 4d) are assigned to (015) and (012) planes of NiAl-LDH, respectively, indicating the formation of the hetero-junction between Bi_2MoO_6 and NiAl-LDH.

Further information about Bi_2MoO_6/LDH-15 was obtained from the EDS results in Fig. 4e, f. The EDX spectra of the samples clearly reveal the existence of Bi, Mo, O, Al and Ni in Bi_2MoO_6/LDH-15 composite. The molar ratio of Ni/Al and Bi/Mo are 0.72:0.24 and 0.39:0.21, respectively, which are close to the theoretical molar ratio of Ni/Al = 3:1 for NiAl-LDH and Bi/Mo = 2:1 for Bi_2MoO_6, further illustrating the formation of the hetero-junction composite between Bi_2MoO_6 and NiAl-LDH.

3.4 UV–Vis analysis

Figure 5a shows the UV–Visible diffuse reflectance spectra of Bi_2MoO_6, NiAl-LDH and Bi_2MoO_6/LDH-15. The data of the
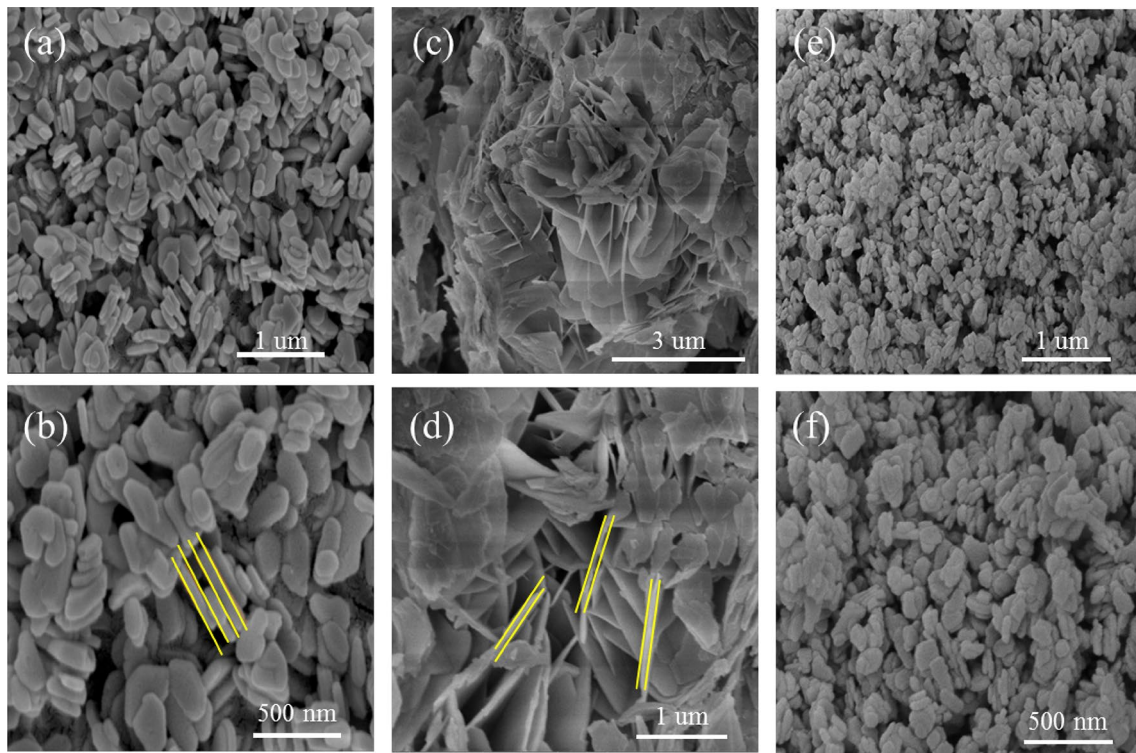

Fig. 2 FT-IR spectra of the samples (a) NiAl-LDH, (b) Bi_2MoO_6, (c) Bi_2MoO_6/LDH-15

Fig. 3 FE-SEM images of the composite **a, b** Bi_2MoO_6, **c, b** NiAl-LDH, **e, f** Bi_2MoO_6/LDH-15 at different resolutions
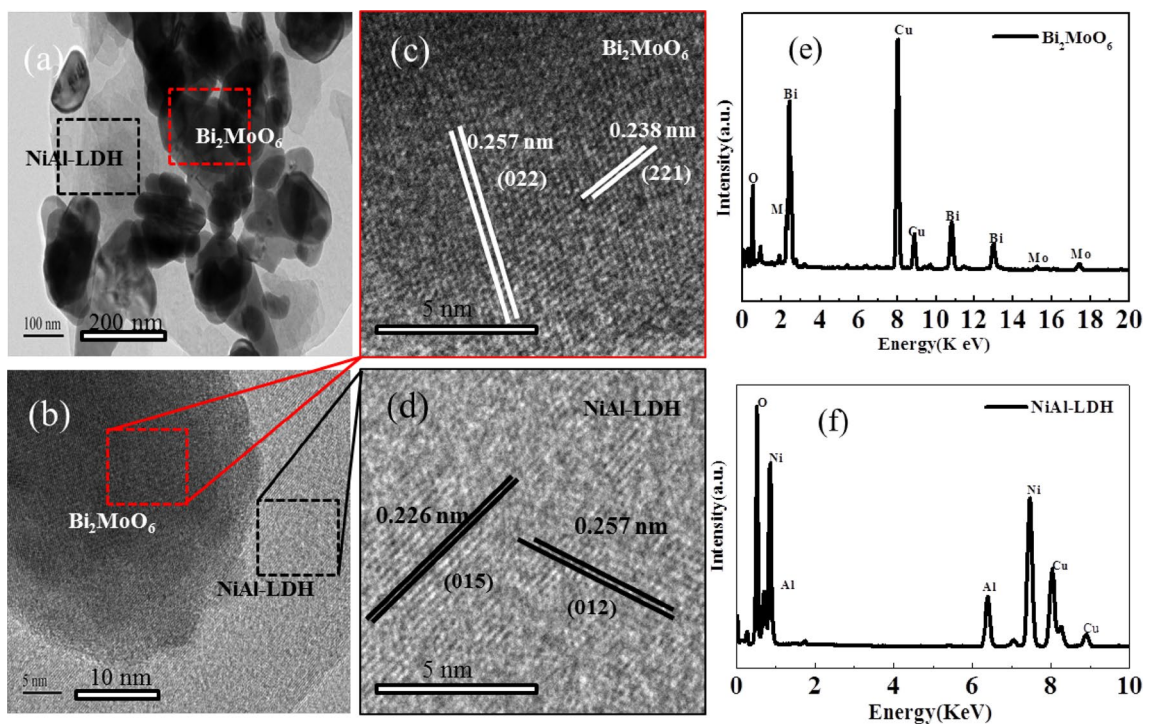

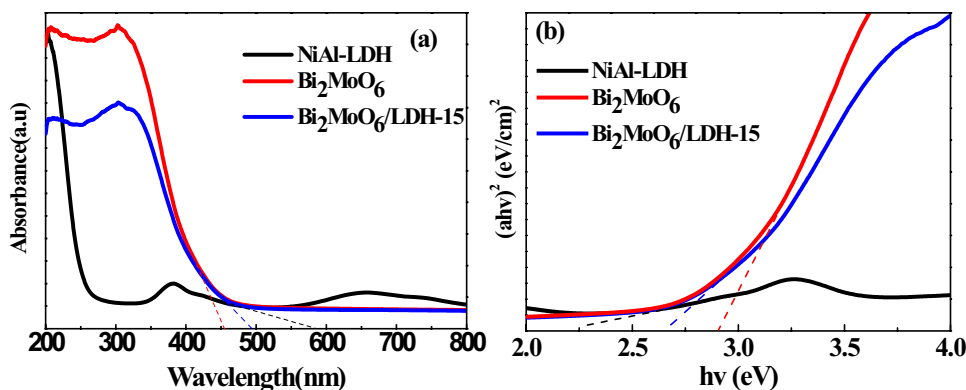**Fig. 4** **a, b** TEM and **a, d** HRTEM images of Bi_2MoO_6/LDH-15, the EDS spectra of **e** NiAl-LDH and **f** Bi_2MoO_6

Fig. 5 a UV–Vis DRS spectra of NiAl-LDH, Bi_2MoO_6 and Bi_2MoO_6/LDH-15 composite, **b** plots of $(\alpha h\nu)^2$ versus energy $(h\nu)$ for Ni Al-LDH, Bi_2MoO_6 and Bi_2MoO_6/LDH

sample measured by UV–Vis spectrophotometer were converted to absorption spectra according to the Kubelka–Munk equation [46, 47]. The optical absorption sidebands of pure Bi_2MoO_6, NiAl-LDH and Bi_2MoO_6/LDH-15 are 450 nm, 570 nm and 495 nm, respectively. The results show that the prepared Bi_2MoO_6/LDH hetero-junction composite can be excited to generate more electron–hole pairs than pure Bi_2MoO_6. In addition, the steep shape of the Bi_2MoO_6/LDH-15 sample spectrum indicates the enhanced visible light absorption, which is attributed to band gap transition [48]. The band gap value of the sample is calculated based on the following equation [48–50]:

$$\alpha h\nu = A\left(h\nu - E_g\right)^{n/2}$$

where α, ν, E_g, h are the absorption coefficient, optical frequency, band gap and Planck's constant, respectively. Figure 5b is the plotted $(\alpha h\nu)^{2/n}$ vs. $h\nu$ spectrum, and Bi_2MoO_6 is a direct transition semiconductor, in which the n value is 1 [51]. The band gap energy of Bi_2MoO_6/LDH-15 hetero-junction ($E_g = 2.65$ eV) is smaller than that of pure Bi_2MoO_6 ($E_g = 2.91$ eV), indicating that NiAl-LDH modify the forbidden band structure of Bi_2MoO_6 so as to enhance its light absorption ability.

3.5 Brunauer–Emmett–Teller (BET) analysis

Figure 6a–c shows N_2 adsorption–desorption isotherms of NiAl-LDH, Bi_2MoO_6 and Bi_2MoO_6/ LDH-15. The NiAl-LDH adsorption isotherm belongs to type IV (capillary

Fig. 6 a–c N_2 adsorption–desorption isotherms and **d–f** the pore size distributions of Ni Al-LDH, Bi_2MoO_6 and Bi_2MoO_6/LDH-15
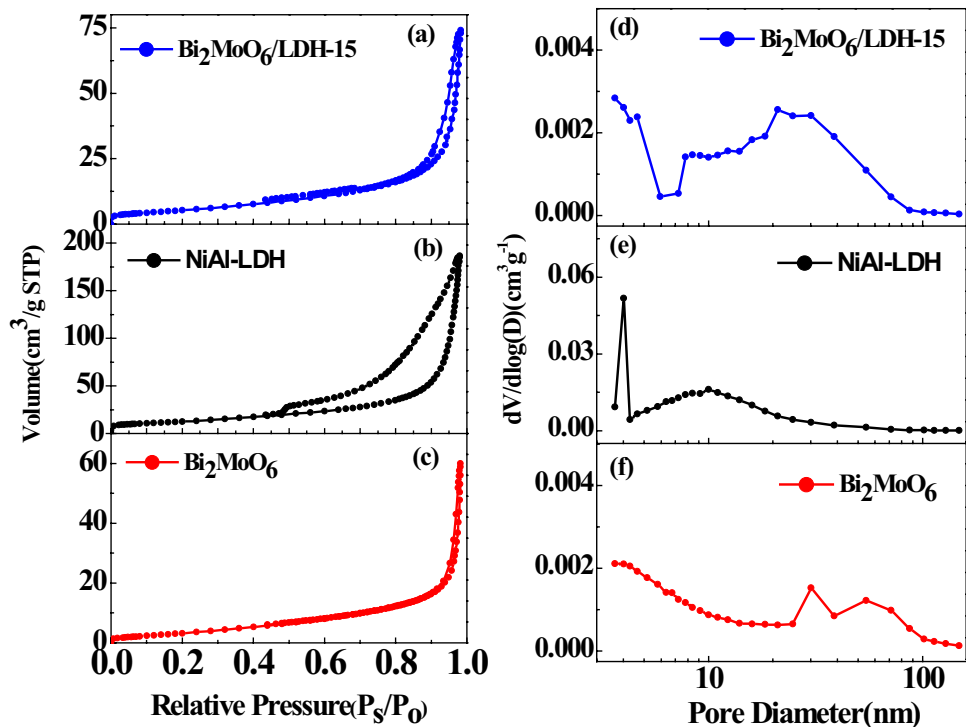
condensation type), of which is H$_1$ type hysteresis loop [52], and Bi$_2$MoO$_6$ and Bi$_2$MoO$_6$/LDH-15 belong to type II [53]. The Brunauer–Emmett–Teller (BET) specific surface areas of NiAl-LDH, Bi$_2$MoO$_6$ and Bi$_2$MoO$_6$/LDH-15 are 24.16, 12.49 and 19.07 m^2 g^{-1}, respectively. The total pore volume of NiAl-LDH, Bi$_2$MoO$_6$ and Bi$_2$MoO$_6$/LDH-15 are 0.155, 0.084 and 0.110 cm^3 g^{-1}. The specific surface area and total pore volume of Bi$_2$MoO$_6$/LDH are slightly larger than that of Bi$_2$MoO$_6$. The larger specific surface area means more exposed active sites and produces more photogenerated charge carriers under visible light illumination. Increased pore volume allows more contaminants to enter the photocatalyst and accelerates the degradation of contaminants. Although the specific surface area and pore volume of the hydrotalcite are large, the recombination rate of photogenerated electron–hole pairs of hydrotalcite is very high, resulting in poor photocatalytic activity.

As shown in Fig. 6d–f, the pore-size distributions of NiAl-LDH, Bi$_2$MoO$_6$ and Bi$_2$MoO$_6$/LDH-15 are calculated based on the Barrett–Joyner–Halenda (BJH) method from the desorption branches of N$_2$ adsorption–desorption isotherms. The most probable pore diameters of NiAl-LDH, Bi$_2$MoO$_6$ and Bi$_2$MoO$_6$/LDH-15 are 10–25, 30–45 and 40 nm, respectively. All of these are characteristic mesopores (2–50 nm). Thus, it can be seen that the NiAl-LDH also has a certain effect on the particle size of Bi$_2$MoO$_6$.

3.6 XPS analysis

The elemental valence and composition of NiAl-LDH, Bi$_2$MoO$_6$ and Bi$_2$MoO$_6$/LDH-15 were further studied by

Fig. 7 The survey spectra and high-resolution XPS spectra of the Ni 2p, Al 2p, Bi 4f, Mo 3d and O 1s regions for NiAl-LDH, Bi$_2$MoO$_6$ and Bi$_2$MoO$_6$/LDH-15
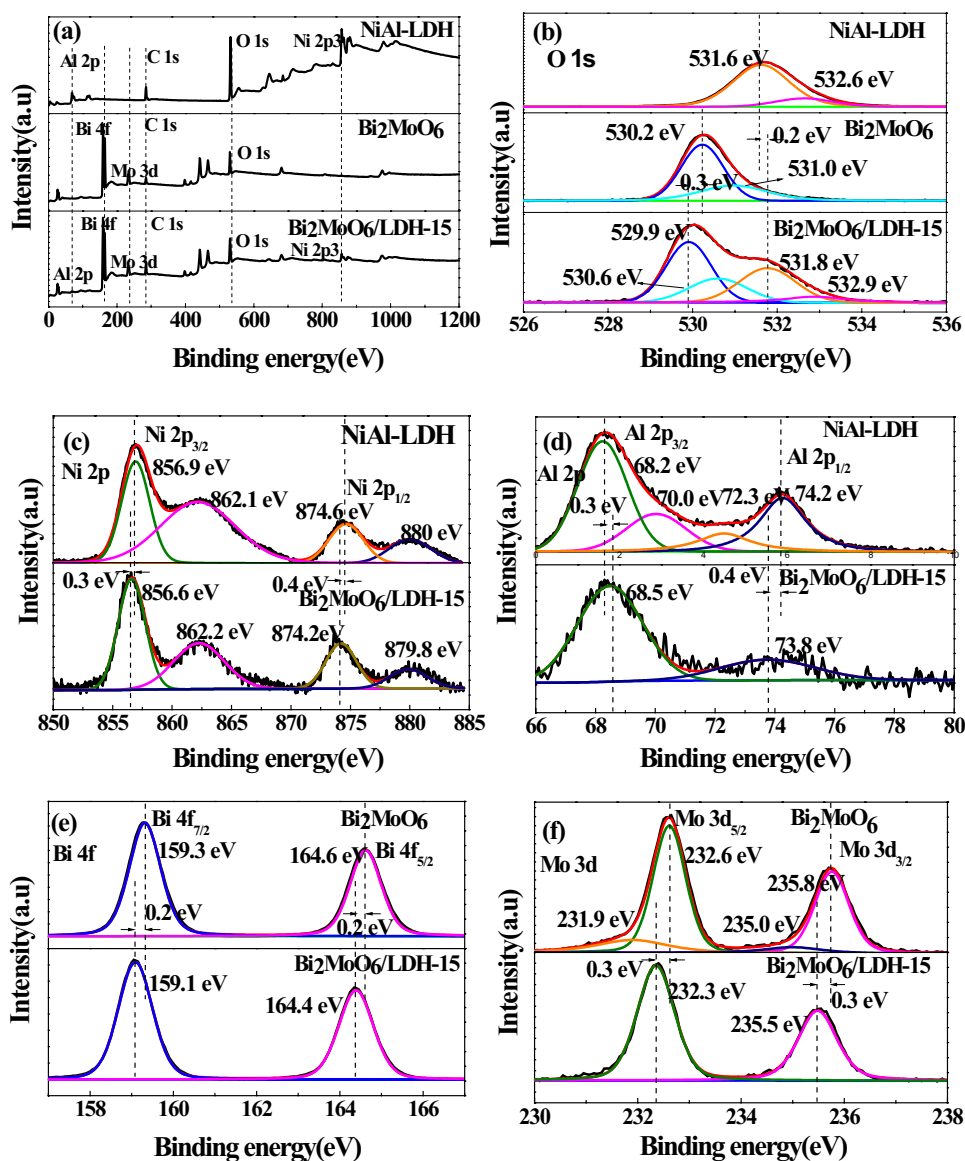
XPS. Figure 7 shows XPS survey spectrum and local high resolution XPS spectra of Ni 2p, Al 2p, Bi 4f, Mo 3d and O 1s of samples. As shown in the survey spectrum (Fig. 7a), Ni 2p, Al 2p, O 1s and C 1s exist on the surface of NiAl-LDH, and Bi 4f, Mo 3d, O 1s and C 1s exist on the surface of Bi_2MoO_6, and Ni 2p, Al 2p, Bi 4f, Mo 3d, O 1s and C 1s exist on the surface of Bi_2MoO_6/LDH-15, indicating the coexistence of NiAl-LDH and Bi_2MoO_6 in Bi_2MoO_6/LDH-15 composite.

As shown in Fig. 7b, two peaks of binding energies around 531.6 eV and 532.6 eV are related to –OH and H_2O in NiAl-LDH spectrum [54], respectively. And the peaks of binding energies of Bi_2MoO_6 at 530.2 eV and 531.0 eV are correlated with Bi–O and Mo–O [29, 55]. The peaks of binding energy of Bi_2MoO_6 /LDH-15 at 529.9 eV, 530.6 eV, 531.3 eV and 532.9 eV are attributed to Bi–O, Mo–O, –OH and H_2O, respectively.

Figure 7c shows the high-resolution spectra of Ni 2p. It is deconvoluted into two peaks around 856.9 eV and 874.6 eV, which are denoted as the Ni $2p_{3/2}$ and Ni $2p_{1/2}$ orbitals of Ni^{2+} [56, 57], which are slightly higher than those of Bi_2MoO_6/LDH-15 at 856.6 eV and 874.2 eV, respectively. Meanwhile, two peaks of NiAl-LDH at 862.1 eV and 880.0 eV and Bi_2MoO_6/LDH-15 at 862.2 eV and 879.8 eV are incidental weak satellite peaks of the Ni $2p_{3/2}$ and Ni $2p_{1/2}$ orbitals, respectively [58].

As shown in Fig. 7d, the Al 2p spectrum shows that the peaks located at the binding energies of 68.2 eV and 74.2 eV are assigned to the Al $2p_{3/2}$ and Al $2p_{1/2}$ orbitals of Al^{3+} in NiAl-LDH [59], which are slightly lower than those of Bi_2MoO_6/LDH-15 at 68.5 eV and 73.8 eV, respectively. Simultaneously, the peaks of NiAl-LDH at 70.0 eV and 72.3 eV are incidental weak satellite peaks of the Al 2p3/2 and Al 2p1/2 orbitals, respectively.

The high-resolution spectra of the Bi 4f in Fig. 7e show that the binding energies of Bi_2MoO_6 at 159.3 eV and 164.6 eV are respectively marked as Bi $4f_{7/2}$ and Bi $4f_{5/2}$ signals of the oxidation state of Bi^{3+} [60, 61], which are slightly higher 0.2 eV than those of Bi_2MoO_6/LDH-15 at 159.1 eV and 164.4 eV, respectively.

The Mo 3d spectrum (Fig. 7f) for Bi_2MoO_6 consists of two peaks of binding energies at 232.6 eV and 235.8 eV, ascribed to Mo $3d_{5/2}$ and Mo $3d_{3/2}$ orbitals of Mo^{6+} in MoO_6 [60], which are slightly higher 0.3 eV than those of Bi_2MoO_6/LDH-15 at 232.3 eV and 235.5 eV, respectively.

The changes in binding energies of Ni^{2+}, Al^{3+}, Bi^{3+}, Mo^{6+} indicates a strong interfacial chemical interaction between Bi_2MoO_6 and NiAl-LDH.

3.7 Photocatalytic activity

The visible light photocatalytic performance of NiAl-LDH, Bi_2MoO_6 and Bi_2MoO_6/LDH-15 were evaluated using RhB
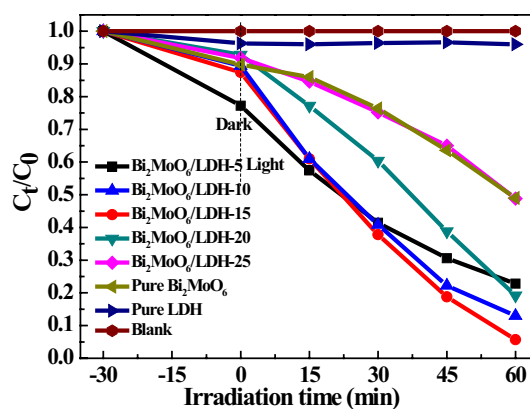
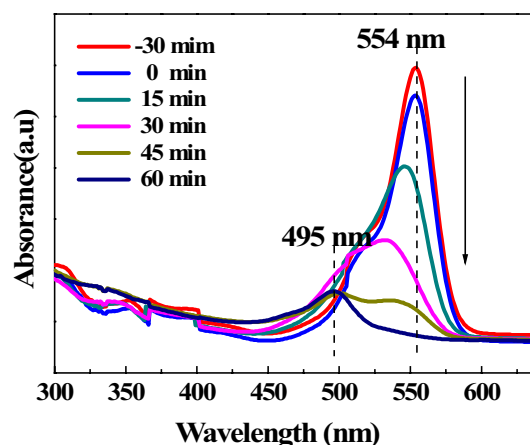**Fig. 8** Photocatalytic degradation of RhB under visible light irradiation

Fig. 9 Absorption spectral changes of RhB solution under visible light irradiation with Bi_2MoO_6/LDH-15

aqueous solution as an organic contamination. Adsorption equilibrium was reached of samples after magnetic stirring for 30 min in the dark (Fig. S2). As shown in Fig. 8, RhB does not self-degrade in the blank test. The RhB concentration was reduced by 5% due to the adsorption of LDH for 60 min under visible light irradiation. For Bi_2MoO_6, the concentration of RhB was reduced by 50% after the visible light irradiation for 60 min. With the LDH amount increase, the photocatalytic activities of Bi_2MoO_6/LDH samples are firstly gradually increased and then decreased with the optimal sample of Bi_2MoO_6/LDH-15. About 95% of RhB can be degraded by Bi_2MoO_6/LDH-15% composite. However, an excess amount of NiAl-LDH may cover the active sites on the surface of Bi_2MoO_6 and there is a great possibility of the development overlapped NiAl-LDH sheets. Thus photogenerated electrons and holes cannot be effectively transferred through Bi_2MoO_6/LDH heterojunction, leading to the reduction of photocatalytic activity. It demonstrates

that an optimized content of NiAl-LDH is crucial for the achievement of excellent activity.

As shown in Fig. 9, the absorption intensity of the contaminant solution at 554 nm is gradually decreased as the illumination time increased. Simultaneously, the maximum absorption wavelength of the contaminant solution is gradually shifted from 554 nm to 495 nm [62]. The blue-shift of the characteristic absorption band indicates the step-by-step de-ethylation of RhB, while the reduced absorbance is attributed to the destruction of the conjugated structure, while the color of the solution is changed from pink to pale yellow [63–65]. If the contaminant solution continues to be illuminated under visible light illumination, these peaks will disappear and finally becomes colorless. It suggests that a complete decolorization of the RhB solution.

As shown in Fig. 10 mM isopropanol (·OH), 10 mM benzoquinone (·O_2^-), 10 mM sodium oxalate (h^+) and 10 mM potassium dichromate (e^-) were added into the reaction solution, respectively. The residual amounts of RhB are 42.8%, 77.4%, 9.1%, and 8.3%, respectively. It indicates that the main active species of photocatalytic degradation are ·OH and ·O_2^-. However, h^+ and e^- are not significant active species.

3.8 Electrochemical analysis and PL analysis

The electrochemical testing was carried out in order to deeply understand the separation and transfer mechanism of photogenerated electron–hole pairs of Bi_2MoO_6/LDH-15 hetero-junction photocatalyst. The transient photocurrent response of NiAl-LDH, Bi_2MoO_6 and Bi_2MoO_6/LDH-15 under dark and visible light illumination is shown in Fig. 11. A higher photocurrent density usually means a higher ability to separate photogenerated electron–hole pairs [66]. The decay of photocurrent indicates that a small number of holes are recombined with electrons. When the separation and
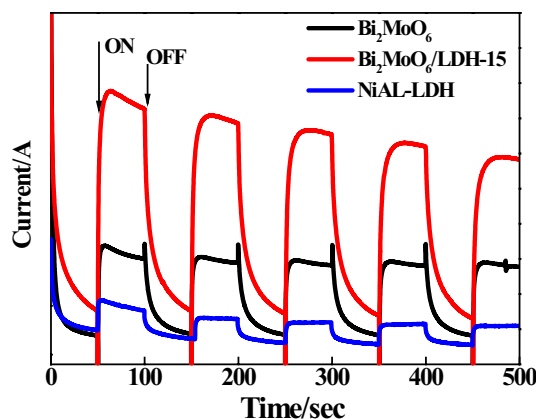

Fig. 11 Transient photocurrent response of NiAl-LDH, Bi_2MoO_6 and Bi_2MoO_6/LDH-15 electrodes in dark and under light irradiation

recombination of electron–hole pairs reaches equilibrium, photocurrent becomes a constant [50]. Pure Bi_2MoO_6 (E_g = 2.91 eV) exhibits a lower intensity photocurrent, while the photocurrent of Bi_2MoO_6/LDH-15 (E_g = 2.65 eV) heterojunction is almost twice that of pure Bi_2MoO_6. It indicates that NiAl-LDH promote the effective separation of photogenerated electron–hole pairs.

The electrochemical impedance spectroscopy (EIS) of NiAl-LDH, Bi_2MoO_6 and Bi_2MoO_6/LDH-15 is shown in Fig. 12. Typically, the radius of arc is related to the charge transfer process at the electrode/electrolyte interface, and the smaller arc in the EIS Nyquist diagram represents a lower charge transfer resistance [67]. The arc radius of Bi_2MoO_6/LDH-15 is smaller than that of NiAl-LDH and Bi_2MoO_6, indicating that Bi_2MoO_6/LDH-15 has small charge transfer resistance and faster electron transport.

Figure S3 is a photoluminescence (PL) spectrum of Bi_2MoO_6 and Bi_2MoO_6/LDH-15, and the lower PL intensity indicates the lower recombination rate of the charge carrier
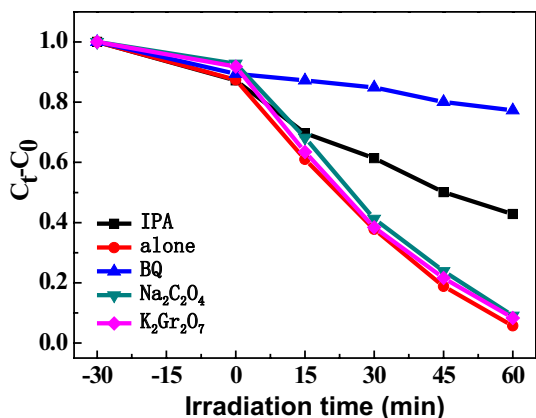

Fig. 10 The effects of reactive species in the degradation of RhB solution under visible light irradiation with Bi_2MoO_6/LDH-15
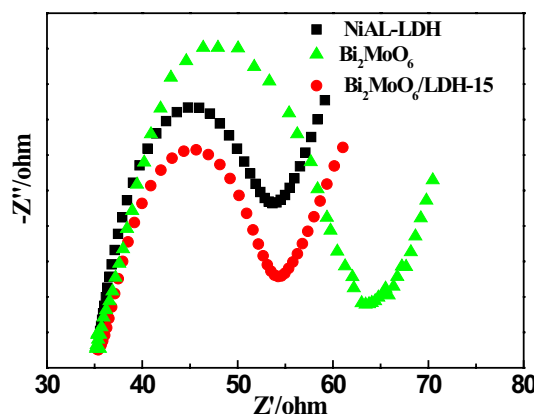

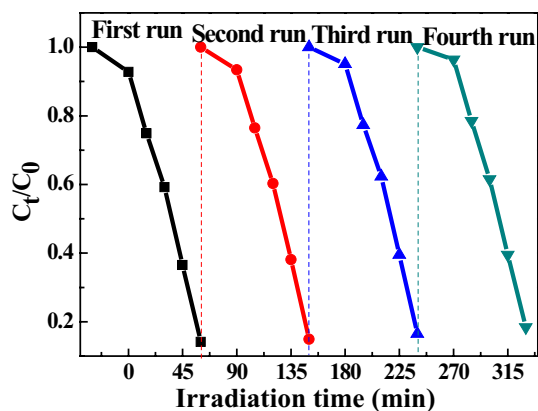**Fig. 12** The EIS Nyquist plots of NiAl-LDH, Bi_2MoO_6 and Bi_2MoO_6/LDH-15 electrodes

Fig. 13 Reuse of Bi_2MoO_6/LDH-15 for the photodegradation of RhB for four successive cycles

[68]. The emission intensity of Bi_2MoO_6/LDH-15 is lower than that of Bi_2MoO_6, indicating that the Bi_2MoO_6/LDH-15 hetero-junction effectively inhibits the recombination of photo-generated electrons and holes.

3.9 Stability and reusability

The stability of the photocatalyst is also an important factor for evaluating photocatalytic performance. The Bi_2MoO_6/LDH-15 sample was selected as the test object. After photocatalytic degradation reaction, the sample was recovered, centrifuged, washed and dried for reuse in the cycle experiment. As shown in Fig. 13, the photocatalytic efficiency results of samples after four cycles are 87.8%, 86.7%, 84.3% and 82.2%, respectively. The photocatalytic performance is slightly reduced due to the loss of photocatalyst and the inactivation of oxidation of a very small portion of the active site of the catalyst. Yet for all that, Bi_2MoO_6/LDH-5 still has good photocatalytic properties, stability and reusability. Fig. S4 shows XRD patterns of Bi_2MoO_6/LDH-5 before and after photocatalytic reaction, indicating that its crystal structure is almost unchanged throughout the reaction except for the change in the intensity of the diffraction peak.

3.10 The photocatalytic mechanism of the Bi_2MoO_6/ LDH composite

Based on the above UV–Vis diffusive reflectance spectra results, the band gap values of NiAl-LDH, Bi_2MoO_6 and Bi_2MoO_6/LDH-15 were calculated to be ~ 2.25 eV, ~ 2.91 eV and ~ 2.65 eV, respectively. The photocatalytic activity enhancement mechanism of composites can be further revealed by estimating the conduction band and valence band potential positions of NiAl-LDH, Bi_2MoO_6 according to the empirical equation [26, 61, 69, 70]:
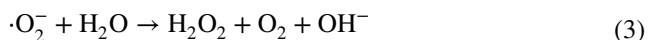
$$E_{VB} = \chi - E_e + 0.5E_g$$

$$E_{CB} = E_{VB} - E_g$$

where χ, E_e and E_g is the absolute electronegativity, the energy of free electrons on the hydrogen scale (~ 4.5 eV), and the band gap energy of the semiconductor, respectively. The χ values of NiAl-LDH and Bi_2MoO_6 are 5.61 eV and 5.17 eV [71, 72], respectively. Thus, the E_{CB} and E_{VB} potentials of NiAl-LDH and Bi_2MoO_6 can be calculated to be -0.02 eV and $+2.23$ eV, as well as -0.78 eV and $+2.13$ eV, respectively. Both NiAl-LDH and Bi_2MoO_6 absorb photons to generate electron–hole pairs. The photo-excited electrons are transported to the conduction band (CB), and leaved holes in the valence band (VB) under visible light irradiation. The electrons of CB of Bi_2MoO_6 are transferred to CB of NiAl-LDH, while the holes of VB of NiAl-LDH are transferred to the VB of Bi_2MoO_6 due to the potential differences so as to effectively reduce the recombination rate of photo-excited electrons and holes (Scheme 1). Figure 10 shows that the addition of isopropanol or benzoquinone causes a greatly change in the photodegradation efficiency of Bi_2MoO_6/LDH, indicating that ·OH and ·O_2^- are significant active species in the photocatalytic process. Because the E ($h^+ = +2.13$ eV) of Bi_2MoO_6 is lower than E (·OH/ $H_2O = +2.68$ eV) [51], photo-induced holes cannot directly oxidize the adsorbed H_2O molecules into ·OH radicals. The E (h^+) is more positive than E (·OH/$OH^- = +1.99$ eV) [73, 74]. The E ($e^- = -0.02$ eV) of NiAl-LDH is more negative than E (O_2/·$O_2^- = +0.13$ eV) [61], and the CB electrons can reduce the dissolved O_2 into ·O_2^- radicals.

According to the above discussion, the probable reactions processes in the photodegradation of RhB are:

$$Bi_2MoO_6 \text{ or LDH} \xrightarrow{h\nu} h^+ + e^- \qquad (1)$$
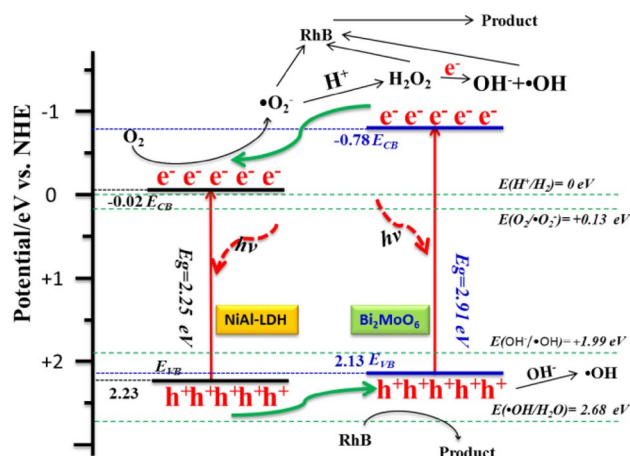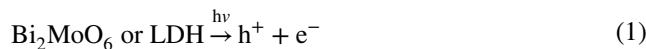
Scheme 1 Schematic diagram of the energy band structure of the Bi_2MoO_6/LDH and the possible charge transfer process under visible light irradiation

$$e^- + O_2 \rightarrow \cdot O_2^- \tag{2}$$

$$\cdot O_2^- + H_2O \rightarrow H_2O_2 + O_2 + OH^- \tag{3}$$

$$H_2O_2 + e^- \rightarrow OH^- + \cdot OH \tag{4}$$

$$h^+ + OH^- \rightarrow \cdot OH \tag{5}$$

$$Bi_2MoO_6(h^+), \cdot O_2^-, \cdot OH + RhB \rightarrow H_2O + CO_2 \tag{6}$$

4 Conclusions

The Bi_2MoO_6/NiAl-LDH hetero-junctions were synthesized by a two-step hydrothermal method with a self-assembled process, in which Bi_2MoO_6 are in-situ intercalated by NiAl-LDH layers. The photocatalytic performance results show that the photocatalytic activity of the synthesized Bi_2MoO_6/NiAl-LDH sample is significantly enhanced, contributing to the synergistic effect between Bi_2MoO_6 and NiAl-LDH. The Bi_2MoO_6/NiAl-LDH exhibits the rapid transfer of photogenerated electrons and the effective separation of electrons and holes on the laminate. The Active species trapping experiment indicates that the $\cdot OH$ and $\cdot O_2^-$ are significant active species in the photocatalytic process. Moreover, the specific surface area and the total pore volume of Bi_2MoO_6/LDH also play a certain roles in Photocatalytic process. According to the photocatalytic stability test, the photocatalytic activity of Bi_2MoO_6/LDH is almost unchanged after repeated cycles. Therefore, Bi_2MoO_6/LDH hetero-junction is a good visible light response photocatalyst with stability and recyclability. Our synthesis method of self-assembly sheets has certain guiding significance for the synthesis and application of other photocatalysts.

Compliance with ethical standards

Conflict of interest All authors have declared that: (i) no support, financial or otherwise, has been received from any organization that may have an interest in the submitted work; and (ii) there are no other relationships or activities that could appear to have influenced the submitted work.

References

1. L.F. Liotta, M. Gruttadauria, G. Di Carlo, G. Perrini, V. Librando, Heterogeneous catalytic degradation of phenolic substrates: catalysts activity. J. Hazard. Mater. **162**, 588–606 (2009)

2. R. Michael, T. Scot, W.Y. Choi, W. Detlef, Environmental applications of semiconductor photocatalysis. Chem. Rev. **95**, 69–96 (1995)

3. C. Liu, C. Zhang, J. Wang, Q. Xu, X. Chen, C. Wang et al., N-doped $CsTi_2NbO_7$ @g-C_3N_4 core-shell nanobelts with enhanced visible light photocatalytic activity. Mater. Lett. **217**, 235–238 (2018)

4. C. Liu, G. Xu, Y. Zhu, Q. Xu, G. Yu, H. Hou et al., In situ construction of layered $K_3Ti_5NbO_{14}$/g-C_3N_4 composite for improving visible-light-driven photocatalytic performance. J. Mater. Sci.: Mater. Electron. **29**, 15859–15868 (2018)

5. Y. Wang, S.K. Li, X.R. Xing, F.Z. Huang et al., Self-assembled 3D flowerlike hierarchical Fe_3O_4@Bi_2O_3 core-shell architectures and their enhanced photocatalytic activity under visible light. Chemistry **17**, 4802–4808 (2011)

6. S. Vadivel, V.P. Kamalakannan, N. Balasubramanian, d-Pencillamine assisted microwave synthesis of Bi_2S_3 microflowers/RGO composites for photocatalytic degradation—a facile green approach. Ceram. Int. **40**, 14051–14060 (2014)

7. F.J. Chen, Y. Cao, D.Z. Jia, Facile synthesis of Bi_2S_3 hierarchical nanostructure with enhanced photocatalytic activity. J. Colloid Interface Sci. **404**, 110–116 (2013)

8. X. Meng, L. Zhang, H.D. Dai, Z.X. Zhao, R.Z. Zhang, Y.X. Liu, Surfactant-assisted hydrothermal fabrication and visible-light-driven photocatalytic degradation of methylene blue over multiple morphological $BiVO_4$ single-crystallites. Mater. Chem. Phys. **125**, 59–65 (2011)

9. W.Z. Yin, W.Z. Wang, L. Zhou, S.M. Sun, L. Zhang, CTAB-assisted synthesis of monoclinic $BiVO_4$ photocatalyst and its highly efficient degradation of organic dye under visible-light irradiation. J. Hazard. Mater. **173**, 194–199 (2010)

10. J. Di, J.X. Xia, Y.P. Ge, H.P. Li et al., Novel visible-light-driven $CQDs$/Bi_2WO_6 hybrid materials with enhanced photocatalytic activity toward organic pollutants degradation and mechanism insight. Appl. Catal. B **168–169**, 51–61 (2015)

11. Z. He, C. Sun, S.G. Yang, Y.C. Ding et al., Photocatalytic degradation of rhodamine B by Bi_2WO_6 with electron accepting agent under microwave irradiation: mechanism and pathway. J. Hazard. Mater. **162**, 1477–1486 (2009)

12. Y.B. Liu, G.Q. Zhu, J.Z. Gao, M. Hojamberdiev et al., A novel CeO_2/$Bi_4Ti_3O_{12}$ composite heterojunction structure with an enhanced photocatalytic activity for bisphenol A. J. Alloys Compd. **688**, 487–496 (2016)

13. Z.W. Chen, H. Jiang, W.L. Jin, C.K. Shi, Enhanced photocatalytic performance over $Bi_4Ti_3O_{12}$ nanosheets with controllable size and exposed {0 0 1} facets for Rhodamine B degradation. Appl. Catal. B **180**, 698–706 (2016)

14. L.M. Reilly, G. Sankar, C.R.A. Catlow, Following the formation of γ-phase Bi_2MoO_6 catalyst by in situ XRD/XAS and thermogravimetric techniques. Solid State Chem. **148**, 178–185 (1999)

15. C. Pirovano, M. Saiful Islam, G. Nowogrocki, G. Mairesse, Modelling the crystal structures of Aurivillius phases. Solid State Ionics **140**, 115–123 (2001)

16. Y. Shimodaira, H. Kobayashi, A. Kudo, Photophysical properties and photocatalytic activities of bismuth molybdates under visible light irradiation. J. Phys. Chem. **110**, 17790–17797 (2006)

17. W. Matthew, M. Patrivk, R. Seshadri, B. Bursten, Structure and bonding in $SnWO_4$, $PbWO_4$, and $BiVO_4$: lone pairs vs inert pairs. Inorg. Chem. **46**, 3839–3850 (2007)

18. H.H. Li, C.Y. Liu, K.W. Li, H. Wang, Preparation, characterization and photocatalytic properties of nanoplate Bi_2MoO_6 catalysts. J. Mater. Sci. **43**, 7026–7034 (2008)

19. Y. Ma, Y. Jia, Z.G. Jiao, M. Yang et al., Hierarchical Bi_2MoO_6 nanosheet-built frameworks with excellent photocatalytic properties. Chem. Commun. (Camb) **51**, 6655–6658 (2015)

20. C.S. Guo, J. Xu, S.F. Wang, L. Li, Y. Zhang, X.C. Li, Facile synthesis and photocatalytic application of hierarchical mesoporous Bi_2MoO_6 nanosheet-based microspheres. CrystEngComm **14**, 3602–3608 (2012)

21. Y. Zheng, F. Duan, J. Wu, M.Q. Liu, Chen, Y. Xie, Enhanced photocatalytic activity of bismuth molybdates with the preferentially exposed {010} surface under visible light irradiation. Mol. Catal. A **303**, 9–14 (2009)

22. Z. Dai, F. Qin, H.P. Zhao, J. Ding, Y.L. Liu, R. Chen, Crystal defect engineering of aurivillius Bi_2MoO_6 by Ce doping for increased reactive species production in photocatalysis. ACS Catal. **6**, 3180–3192 (2016)

23. T.F. Zhou, J.C. Hu, J.L. Li, Er^{3+} doped bismuth molybdate nanosheets with exposed {010} facets and enhanced photocatalytic performance. Appl. Catal. B **110**, 221–230 (2011)

24. R. Adhikari, B. Joshi, R. Narro-García, E. De la Rosa, Microwave hydrothermal synthesis and infrared to visible upconversion luminescence of Er^{3+}/Yb^{3+} co-doped bismuth molybdate nanopowder. J. Lumin. **145**, 866–871 (2014)

25. S.S. Jin, H.S. Hao, Y.J. Gan, W.H. Guo et al., Preparation and improved photocatalytic activities of Ho^{3+}/Yb^{3+} co-doped Bi_2MoO_6. Mater. Chem. Phys. **199**, 107–112 (2017)

26. T. Yan, H.G. Liu, T.T. Wu, X.J. Liu et al., Fabrication of hierarchical $BiOI/Bi_2MoO_6$ heterojunction for degradation of bisphenol A and dye under visible light irradiation. Alloys Compd. **634**, 223–231 (2015)

27. Y.S. Xu, Z.J. Zhang, W.D. Zhang, Facile preparation of heterostructured Bi_2O_3/Bi_2MoO_6 hollow microspheres with enhanced visible-light-driven photocatalytic and antimicrobial activity. Mater. Res. Bull. **48**, 1420–1427 (2013)

28. Y.S. Xu, W.D. Zhang, Anion exchange strategy for construction of sesame-biscuit-like $Bi_2O_2CO_3/Bi_2MoO_6$ nanocomposites with enhanced photocatalytic activity. Appl. Catal. B **140–141**, 306–316 (2013)

29. H.P. Li, J.Y. Liu, W.G. Hou, N. Du et al., Synthesis and characterization of $g-C_3N_4/Bi_2MoO_6$ heterojunctions with enhanced visible light photocatalytic activity. Appl. Catal. B **160–161**, 89–97 (2014)

30. K.M. Parida, L. Mohapatra, Carbonate intercalated Zn/Fe layered double hydroxide: a novel photocatalyst for the enhanced photo degradation of azo dyes. Chem. Eng. J. **179**, 131–139 (2012)

31. L. Mohapatra, K.M. Parida, Zn–Cr layered double hydroxide: visible light responsive photocatalyst for photocatalytic degradation of organic pollutants. Sep. Purif. Technol. **91**, 73–80 (2012)

32. M. Dinari, M.M. Momeni, Y. Ghayeb, Photodegradation of organic dye by ZnCrLa-layered double hydroxide as visible-light photocatalysts. J. Mater. Sci.: Mater. Electron. **27**, 9861–9869 (2016)

33. Y. Fu, F.Y. Ning, S.M. Xu, H.L. An, M.F. Shao, M. Wei, Terbium doped ZnCr-layered double hydroxides with largely enhanced visible light photocatalytic performance. J. Mater. Chem. A **4**, 3907–3913 (2016)

34. N. Gu, J.L. Gao, K.T. Wang, B. Li, W.C. Dong, Y.L. Ma, Microcystis aeruginosa inhibition by Zn–Fe–LDHs as photocatalyst under visible light. J. Taiwan Inst. Chem. Eng. **64**, 189–195 (2016)

35. M. Gong, Y.G. Li, H.L. Wang, Y.G. Liang, J.Z. Wu et al., An advanced Ni-Fe layered double hydroxide electrocatalyst for water oxidation. J. Am. Chem. Soc. **135**, 8452–8455 (2013)

36. J.F. Ma, J.F. Ding, L.M. Yu, L.Y. Li, Y. Kong, S. Komarneni, BiOCl dispersed on NiFe–LDH leads to enhanced photo-degradation of Rhodamine B dye. Appl. Clay Sci. **109–110**, 76–82 (2015)

37. S. Nayak, L. Mohapatra, K. Parida, Visible light-driven novel $g-C_3N_4/NiFe$-LDH composite photocatalyst with enhanced photocatalytic activity towards water oxidation and reduction reaction. J. Mater. Chem. A **3**, 18622–18635 (2015)

38. M. Mureseanu, T. Radu, R.D. Andrei, M. Darie, G. Carja, Green synthesis of $g-C_3N_4$/CuONP/LDH composites and derived $g-C_3N_4$/MMO and their photocatalytic performance for phenol reduction from aqueous solutions. Appl. Clay Sci. **141**, 1–12 (2017)

39. X. Zhao, T.G. Xu, W.Q. Yao, Y.F. Zhu, Photodegradation of dye pollutants catalyzed by $\gamma-Bi_2MoO_6$ nanoplate under visible light irradiation. Appl. Surf. Sci. **255**, 8036–8040 (2009)

40. F. Chen, C.G. Niu, Q. Yang, X.M. Li, G.G. Zeng, Facile synthesis of visible-light-active BiOI modified Bi_2MoO_6 photocatalysts with highly enhanced photocatalytic activity. Ceram. Int. **42**, 2515–2525 (2016)

41. N. Tian, H.W. Huang, Y.X. Guo, Y. He, Y.H. Zhang, $Ag-C_3N_4/Bi_2O_2CO_3$ composite with high visible-light-driven photocatalytic activity for rhodamine B degradation. Appl. Surf. Sci. **322**, 249–254 (2014)

42. W.J. Wang, H.F. Cheng, B.B. Huang, X.J. Lin et al., Synthesis of $Bi_2O_2CO_3/Bi_2S_3$ hierarchical microspheres with heterojunctions and their enhanced visible light-driven photocatalytic degradation of dye pollutants. J. Colloid Interface Sci. **402**, 34–39 (2013)

43. Y.P. Zhu, M.W. Laipan, R.L. Zhu, T.Y. Xu et al., Enhanced photocatalytic activity of Zn/Ti-LDH via hybridizing with C60. Mol. Catal. **427**, 54–61 (2017)

44. J.M. Ferna´ndez, C. Barriga, M.A. Ulibarri, F.M. Labajos, V. Rives, New hydrotalcite-like compounds containing yttrium. Chem. Mater. **9**, 312–318 (1997)

45. J. Li, F.P. Chen, G.P. Jin, X.S. Feng, X.X. Li, Removals of aqueous sulfur dioxide and hydrogen sulfide using CeO_2-NiAl-LDHs coating activated carbon and its mix with carbon nano-tubes. Colloids Surf. A **476**, 90–97 (2015)

46. Y. Izum, T. Itoi, S. Peng, K. Oka, Y. Shibata, Site structure and photocatalytic role of sulfur or nitrogen-doped titanium oxide with uniform mesopores under visible light. J. Phys. Chem. **113**, 6706–6718 (2009)

47. Q.M. Zhao, Q. Zhang, J.Q. Huang, F. Wei, Hierarchical nanocomposites derived from nanocarbons and layered double hydroxides—properties, synthesis, and applications. Adv. Funct. Mater. **22**, 675–694 (2012)

48. X.T. Gao, E. Wachs Israel, Investigation of surface structures of supported vanadium oxide catalysts by UV-vis-NIR diffuse reflectance spectroscopy. J. Phys. Chem. **104**, 1261–1268 (2000)

49. G.K. Mikami, F. Grosu, S. Kawamura, Y. Yoshida, G. Carja, Y. Izumi, Harnessing self-supported Au nanoparticles on layered double hydroxides comprising Zn and Al for enhanced phenol decomposition under solar light. Appl. Catal. B **199**, 260–271 (2016)

50. M.Y. Zhang, C.L. Shao, P. Zhang, C.Y. Su, X. Zhang, Bi_2MoO_6 microtubes: controlled fabrication by using electrospun polyacrylonitrile microfibers as template and their enhanced visible light photocatalytic activity. J. Hazard. Mater. **225–226**, 155–163 (2012)

51. C.I. Ezeh, M.C. Tomatis, X.G. Yang, J. He, C.G. Sun, Ultrasonic and hydrothermal mediated synthesis routes for functionalized Mg-Al LDH: comparison study on surface morphology, basic site strength, cyclic sorption efficiency and effectiveness. Ultrason. Sonochem. **40**, 341–352 (2018)

52. A. Martínez-de la Cruz, S. Obregón Alfaro, Synthesis and characterization of $\gamma-Bi_2MoO_6$ prepared by co-precipitation: photoassisted degradation of organic dyes under vis-irradiation. J. Mol. Catal. A **320**, 85–91 (2010)

53. X.W. Lv, X. Xiao, M.L. Cao, Y. Bu, C. Wang et al., Efficient carbon dots/NiFe-layered double hydroxide/BiVO 4 photoanodes for photoelectrochemical water splitting. Appl. Surf. Sci. **439**, 1065–1071 (2018)

54. J.L. Lv, K. Dai, J.F. Zhang, L. Geng, C.H. Liang et al., Facile synthesis of Z-scheme graphitic-C_3N_4/Bi_2MoO_6 nanocomposite

for enhanced visible photocatalytic properties. Appl. Surf. Sci. **358**, 377–384 (2015)

55. M.F. Shao, F.Y. Ning, J. Zhao, M. Wei, D.G. Evans, X. Duan, Preparation of $Fe_3O_4@SiO_2@$ layered double hydroxide core-shell microspheres for magnetic separation of proteins. J. Am. Chem. Soc. **134**, 1071–1077 (2012)

56. X.H. Huang, G.H. Li, B.Q. Cao, M. Wang, C.Y. Hao, Morphology evolution and CL property of Ni-doped zinc oxide nanostructures with room-temperature ferromagnetism. J. Phys. Chem. **113**, 4381–4385 (2009)

57. S. Tonda, S. Kumar, M. Bhardwaj, P. Yadav, S. Ogale, g-C_3N_4/NiAl-LDH 2D/2D hybrid heterojunction for high-performance photocatalytic reduction of CO_2 into renewable fuels. ACS Appl. Mater. Interfaces **10**, 2667–2678 (2018)

58. X. Lu, J. Ma, H.X. Jiang, C. Liu, K.M. Lau, Low trap states in in situ SiNx/AlN/GaN metal-insulator-semiconductor structures grown by metal-organic chemical vapor deposition. Appl. Phys. Lett. **105**, 102911–102915 (2014)

59. J.H. Bi, L. Wu, J. Li, Z.H. Li, X.X. Wang, X.Z. Fu, Simple solvothermal routes to synthesize nanocrystalline Bi_2MoO_6 photocatalysts with different morphologies. Acta Mater. **55**, 4699–4705 (2007)

60. X. Du, J. Wan, J. Jia, C. Pan, X.Y. Hu et al., Photocatalystic degradation of RhB over highly visible-light-active Ag_3PO_4-Bi_2MoO_6 heterojunction using H_2O_2 electron capturer. Mater. Design **119**, 113–123 (2017)

61. L. Zhang, D.R. Chen, X.L. Jiao, Monoclinic structured $BiVO_4$ nanosheets: hydrothermal preparation, formation mechanism, and coloristic and photocatalytic properties. J. Phys. Chem. **110**, 2668–2673 (2006)

62. C. Zhang, Y.F. Zhu, Synthesis of square Bi_2WO_6 nanoplates as high-activity visible-light-driven photocatalysts. Chem. Mater. **17**, 3537–3545 (2005)

63. T. Yan, Q. Yan, X.D. Wang, H.Y. Liu, M.M. Li et al., Facile fabrication of heterostructured g-C_3N_4/Bi_2MoO_6 microspheres with highly efficient activity under visible light irradiation. Dalton Trans. **44**, 1601–1611 (2015)

64. C. Liu, H.J. Zhu, Y.S. Zhu, P.Y. Dong, H.J. Hou et al., Ordered layered N-doped $KTiNbO_5$/g-C_3N_4 heterojunction with enhanced visible light photocatalytic activity. Appl. Catal. B **228**, 54–63 (2018)

65. W. Wang, J.J. Fang, S.F. Shao, M. Lai, C.H. Lu, Compact and uniform $TiO_2@g$-C_3N_4 core-shell quantum heterojunction for photocatalytic degradation of tetracycline antibiotics. Appl. Catal. B **217**, 57–64 (2017)

66. C. Liu, Q.S. Wu, M.W. Ji, H.J. Zhu et al., Constructing Z-scheme charge separation in 2D layered porous BiOBr/graphitic C_3N_4 nanosheets nanojunction with enhanced photocatalytic activity. J. Alloys Compd. **723**, 1121–1131 (2017)

67. Z. Lu, L. Zeng, W.L. Song, Z. Qin, D.W. Zeng, C.S. Xie, In situ synthesis of C-TiO_2/g-C_3N_4 heterojunction nanocomposite as highly visible light active photocatalyst originated from effective interfacial charge transfer. Appl. Catal. B **202**, 489–499 (2017)

68. F. Dong, Y.H. Li, Z.Y. Wang, W.K. Ho, Enhanced visible light photocatalytic activity and oxidation ability of porous graphene-like g-C_3N_4 nanosheets via thermal exfoliation. Appl. Surf. Sci. **358**, 393–403 (2015)

69. Y. Xu, A.A. Martin, The absolute energy positions of conduction and valence bands of selected semiconducting minerals. Am. Miner. **85**, 543–556 (2000)

70. C.N. Tang, E.Z. Liu, J. Wan, X.Y. Hu, J. Fan, Co_3O_4 nanoparticles decorated Ag_3PO_4 tetrapods as an efficient visible-light-driven heterojunction photocatalyst. Appl. Catal. B **181**, 707–715 (2016)

71. R.G. Pearson, Absolute electronegativity and hardness: application to inorganic chemistry. Inorg. Chem. **27**, 734–740 (1988)

72. D.C. Ghosh, T. Chakraborty, Gordy's electrostatic scale of electronegativity revisited. J. Mol. Struct. Theochem **906**, 87–93 (2009)

73. D. Kandi, S. Martha, A. Thirumurugan, K.M. Parida, CdS QDs-decorated self-doped γ-Bi_2MoO_6: a sustainable and versatile photocatalyst toward photoreduction of Cr(VI) and degradation of phenol. ACS OMEGA **2**, 9040–9056 (2017)

74. C. Liu, R.R. Han, H.M. Ji, T. Sun, J. Zhao et al., S-doped mesoporous nanocomposite of $HTiNbO_5$ nanosheets and TiO_2 nanoparticles with enhanced visible light photocatalytic activity. Phys. Chem. Chem. Phys. **18**, 801–810 (2016)